Superconductor
Science and
Technology

LETTER

Analysis of thermal grooving effects on vortex penetration in vapor-diffused Nb_3Sn

To cite this article: Eric M Lechner *et al* 2025 *Supercond. Sci. Technol.* **38** 01LT01

Letters

IOP Publishing

Superconductor Science and Technology

Supercond. Sci. Technol. **38** (2025) 01LT01 (8pp)

https://doi.org/10.1088/1361-6668/ad9416

Letter

Analysis of thermal grooving effects on vortex penetration in vapor-diffused Nb_3Sn

Eric M Lechner[1,*], Olga Trofimova[1], Jonathan W Angle[2], Madison C DiGuilio[3] and Uttar Pudasaini[1,*]

[1] Thomas Jefferson National Accelerator Facility, Newport News, VA 23606, United States of America
[2] Pacific Northwest National Laboratory, Richland, WA 99354, United States of America
[3] Tidewater Community College, Norfolk, VA 23510, United States of America

E-mail: lechner@jlab.org and uttar@jlab.org

Received 20 August 2024, revised 20 October 2024
Accepted for publication 17 November 2024
Published 27 November 2024

Abstract

While Nb_3Sn theoretically offers better superconducting radio-frequency (RF) cavity performance (Q_0 and E_{acc}) to Nb at any given temperature, peak RF magnetic fields consistently fall short of the ∼400 mT prediction. The relatively rough topography of vapor-diffused Nb_3Sn is widely conjectured to be one of the factors that limit the attainable performance of Nb_3Sn-coated Nb cavities prepared via Sn vapor diffusion. Here we investigate the effect of coating duration on the topography of vapor-diffused Nb_3Sn on Nb and calculate the associated magnetic field enhancement and superheating field suppression factors using atomic force microscopy topographies. It is shown that the thermally grooved grain boundaries are major defects which may contribute to a substantial decrease in the achievable accelerating field. The severity of these grooves increases with total coating duration due to the deepening of thermal grooves during the coating process.

Keywords: superconducting radio frequency, vortex nucleation, atomic force microscopy, superheating field

Radio-frequency (RF) cavities are electromagnetic resonators capable of storing electromagnetic energy to accelerate charged particle beams in modern accelerators. Compared with normal conducting RF cavities, superconducting RF (SRF) cavities possess much smaller surface resistance, R_s, reducing the RF power dissipation in the cavity walls by 5–6 orders of magnitude compared to normal conducting materials. This low surface resistance allows SRF cavities to operate at high fields in continuous wave mode. Bulk niobium ($T_c \approx 9.2$ K, $B_c \approx 200$ mT, $B_{sh} \approx 240$ mT, and $\Delta \approx 1.5$ meV [1–4]) is currently the material of choice to fabricate SRF cavities due to its superior superconducting properties among the pure elements and suitable mechanical properties to form complex structures. Over the past five decades, continual research and development has advanced Nb SRF cavity technology, determining performance limiting mechanisms, and developing adequate processes to mitigate them.

Niobium cavities often require operating at ∼2 K for optimal performance, which demands complicated cryogenic facilities, and is a major cost driver for SRF-based accelerators. Nb_3Sn is an alternative material with potential to surpass the state-of-art Nb cavity performance. Nb_3Sn possesses superior superconducting properties: $T_c \approx 18.3$ K, $B_c \approx$

* Authors to whom any correspondence should be addressed.

470 mT, $B_{sh} \approx 400$ mT, and $\Delta \approx 3.4$ meV [5–8], all almost twice that of Nb. Theoretically, it promises higher accelerating gradient, quality factor, and operating temperature than bulk Nb. Nb_3Sn SRF cavities at 4.3 K can deliver similar performance to Nb cavities at 2 K. This would enable enormous cost savings for future SRF accelerators by simplifying cryogenic facilities and reducing their operating cost. Successful deployment of Nb_3Sn technology would usher in an era of high efficiency conduction-cooled accelerators for basic science, medicinal and industrial applications [9, 10].

Nb_3Sn cavities routinely operate at peak magnetic fields between B_{c1} and B_{sh}, indicating B_{c1} is not a limiting parameter for the operation in the metastable Meissner state. It has been shown using both DC and short high power pulses that a major limitation may be related to flux penetration at defects in the RF layer [11]. While Nb_3Sn theoretically offers superior peak accelerating fields, they are typically limited below 20 MV m^{-1} (85 mT) [12]. To date, the highest accelerating gradient at 4.2 K in vapor-diffused Nb_3Sn 1.3 GHz single cell cavities is 24 MV m^{-1} (100 mT) [13]. An interesting observation from witness sample studies of that cavity showed unusually small surface roughness.

The smoothness of the RF surface is one of the important aspects to achieve high-field cavity performance. Smoother is better. As such, an ideal surface is perfectly flat. Surface roughness on a superconductor exposed to an applied magnetic field introduces two vulnerabilities to the preservation of the Meissner state: magnetic field enhancement (MFE) and superheating field suppression (SFS). MFE arises from the supercurrent screening of applied magnetic fields by rough surfaces where the magnetic field is locally increased. The most severely affected regions are marked by sharp edge/small radius of curvature topographic defects [14–18]. The local field due to MFE can exceed the critical magnetic field of the material and cause regions of the defect to transit into the normal conducting state. These normal conducting regions expand and lead to thermal instability [14, 15, 19, 20]. Localized SFS, a weakened stability of the metastable Meissner state, arises due to nanoscale roughness [21–23]. This weakened stability results from the competition between the external magnetic field pushing a vortex into the superconductor and the image force from the surface expelling it. Topographic defects facilitate premature breakdown of the metastable Meissner state by enhancing the force from the external magnetic field pushing a vortex into the surface due to current crowding, a concept familiar to optimization of superconducting nanocircuits [24, 25], and reducing the force from the surface expelling it [22]. At B_{sh} the surface is absolutely unstable to nucleation of highly dissipative vortices that may contribute to thermal instability [26–28]. Recent analysis of N-doped and low temperature baked Nb showed that the preservation of B_{sh} may play a role in experimentally attainable peak field [29, 30].

In this work the effect of coating duration on the topography of Sn vapor-diffused Nb_3Sn samples and its implications on SFS and MFE is investigated. Nb_3Sn coatings were prepared using a similar Sn vapor diffusion process used to coat Nb_3Sn on Nb cavities. The samples were prepared during a study to elucidate the growth mechanism of Nb_3Sn coating during the vapor diffusion process [31]. This coating consists of two steps: nucleation and growth. Tin chloride is first evaporated at ~500 °C, depositing a Sn film and particles onto the Nb surface to mitigate non-uniformity in the coating by improving nucleation [32]. The Nb_3Sn growth temperature was 1200 °C, well above the temperature of 930 °C needed to exclusively form the Nb_3Sn phase. Topographic measurements were acquired using a Dimension Icon Atomic Force Microscope, Bruker, at the Applied Research Center Core Labs of College of William and Mary. All measurements were made in tapping mode (TMAFM), using scanasyst-air probes (Bruker) [33] at 512 × 512 pixels. As grown vapor-diffused Nb_3Sn surfaces are topographically imperfect. A representative Nb_3Sn surface is shown in figure 1(a). Grain boundaries host high slope angle grooves as highlighted by the secondary electron scanning electron microscopy (SE-SEM) image, line profile through the topography in (a) and high angle annular dark field scanning transmission electron microscopy (HAADF-STEM) shown in figures 1(b)–(d). The surface is

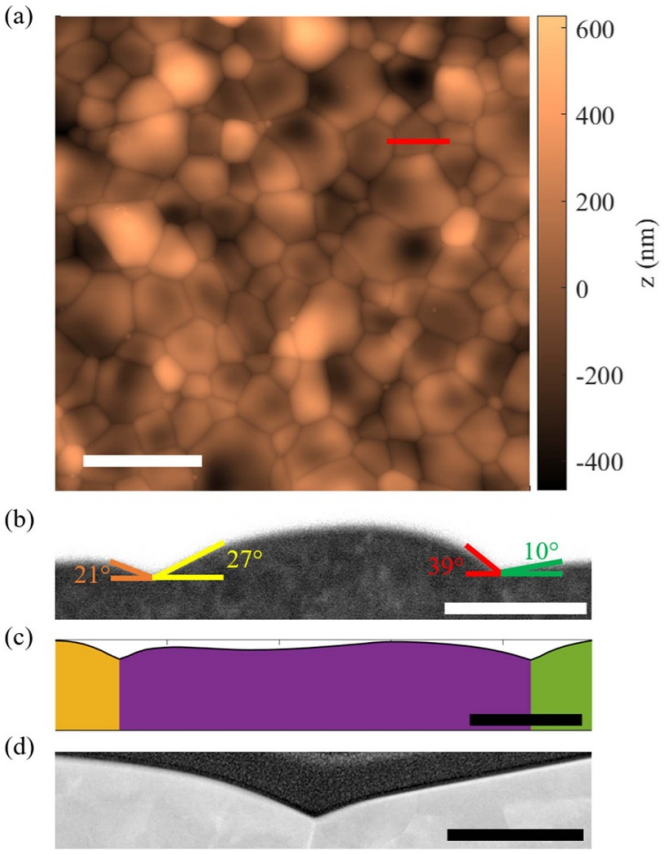

Figure 1. (a) Representative TMAFM topography of a Nb_3Sn surface after 6 h of coating time at $T = 1200$ °C. The scale bar is 5 μm. (b) SE-SEM image of a cross-section through a grain. The scale bar is 1 μm. (c) Topographic line profile through the area marked by the red line in (a). Grains are marked by different colors beneath the topographic line profile. The scale bar is 500 nm. (d) HAADF-STEM image of a grain boundary groove cross-section. The scale bar is 200 nm.

characterized by an undulating intragranular topography separated by V-shaped, grooved grain boundaries. The grooved grain boundaries are qualitatively consistent with the shape of thermal grooving via surface diffusion [34, 35]. The groove root, which should retain a self-similar shape during growth [34], is sharp as shown in figure 1(d). These topographic defects give rise to local MFE and SFS. The MFE and SFS factors, $\beta(\mathbf{r})$ and $\eta(\mathbf{r})$, are defined by $B(\mathbf{r}) = \beta(\mathbf{r})B_0$ and $B^*_{\rm sh}(\mathbf{r}) = \eta(\mathbf{r})B_{\rm sh}$, respectively. Here B_0 is the magnetic field far from the surface, $B(\mathbf{r})$ is the local magnetic field, $B_{\rm sh}$ is the superheating field of a perfectly flat surface and $B^*_{\rm sh}(\mathbf{r})$ is the geometrically modified superheating field. The MFE and SFS factors were calculated using the perfect electrical conductor model [29] and considering a triangular groove geometry similar to the one proposed by Kubo [22] to calculate SFS, as shown in figure 2(a). In this simple model, we consider the competition between the force of the external magnetic field, $\mathbf{F_M}$, driving a vortex into the surface and the image vortex force, $\mathbf{F_S}$, expelling it from the surface. The force from the external magnetic field is given by

$$\mathbf{F_M} = \mathbf{J_M} \times \phi_0 \hat{\mathbf{z}} \tag{1}$$

and the force from the surface is determined by the interaction with the image vortex given by

$$\mathbf{F_S} = \mathbf{J_I} \times \phi_0 \hat{\mathbf{z}}, \tag{2}$$

where $\mathbf{J_M} = \nabla \times \mathbf{B}/\mu_0$ is determined by solution of the London equation of an infinitely long triangular groove defect aligned in the z direction. In this case the solution, $\mathbf{B}(x,y)$, lies only in the z direction leading to the governing equation

$$\nabla^2 B_z = \frac{1}{\lambda^2} B_z, \tag{3}$$

where λ is the London penetration depth with the boundary conditions $\mathbf{B}(x, y = h(x)) = B_0\hat{z}$, $\mathbf{B}(x, y = \infty) = 0$ and $\nabla B_z \cdot \hat{\mathbf{x}} = 0$. Where $h(x)$ defines the surface contour. $\mathbf{J_I} = -\nabla\Phi_I$, where Φ_I is the current density scalar potential of the image vortex calculated via conformal mapping

$$\frac{2\pi\mu_0\lambda^2}{\phi_0}\Phi_I(x,y) = \tilde{\Phi}_I(x,y) = \mathrm{Re}\left(-i\ln\left(w - w_0^*\right)\right)|_{w=F^{-1}(x,y)}, \tag{4}$$

w is the complex coordinate, w_0^* is the complex conjugate of the vortex nucleation position in the w-plane which preserves the boundary condition of zero normal current density to the surface, and F^{-1} is the inverse map between w and real coordinate calculated numerically and described in detail elsewhere [22]. Here the coherence length, ξ, is used as the cutoff length scale in the London theory [22, 36]. When the sum of the forces on the vortex vanishes, $\mathbf{F_S} + \mathbf{F_M} = \mathbf{0}$, the Bean–Livingston barrier becomes unstable to vortex penetration [22] which leads to the following expression

$$B^*_{\rm sh} = \frac{2\xi|-\nabla\tilde{\Phi}_I(\mathbf{r_v})|}{\epsilon(\mathbf{r_v})}B_{\rm sh}, \tag{5}$$

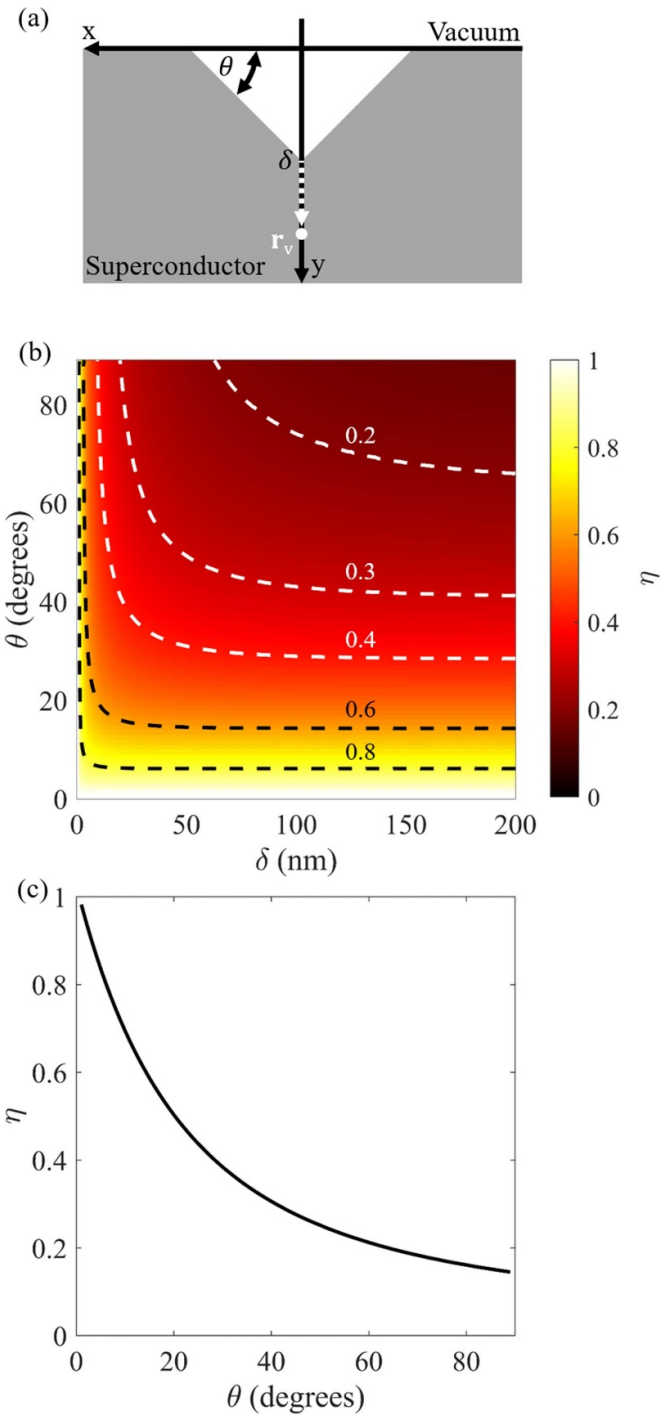

Figure 2. (a) Triangular groove geometry used in the SFS model. (b) Color plot of $\eta(\delta,\theta)$ via equation (6). (c) $\eta(\theta)$ in the deep-groove limit. $\xi = 3$ nm and $\lambda = 120$ nm were used to represent Nb_3Sn.

where $B_{\rm sh} = \phi_0/4\pi\lambda\xi$ is the superheating field of a perfectly flat surface in the London theory, $\epsilon(\mathbf{r}) = |\mathbf{J}(\mathbf{r})|/J_0$ is the local current density enhancement factor, and $\mathbf{r_v}$ is the vortex nucleation position given by $\mathbf{r_v} = (\delta + \xi)\hat{\mathbf{y}}$ for this geometry. This defines the SFS factor

$$\eta(\xi,\lambda,\delta,\theta) = \frac{2\xi|-\nabla\tilde{\Phi}_I(\mathbf{r_v})|}{\epsilon(\mathbf{r_v})}, \tag{6}$$

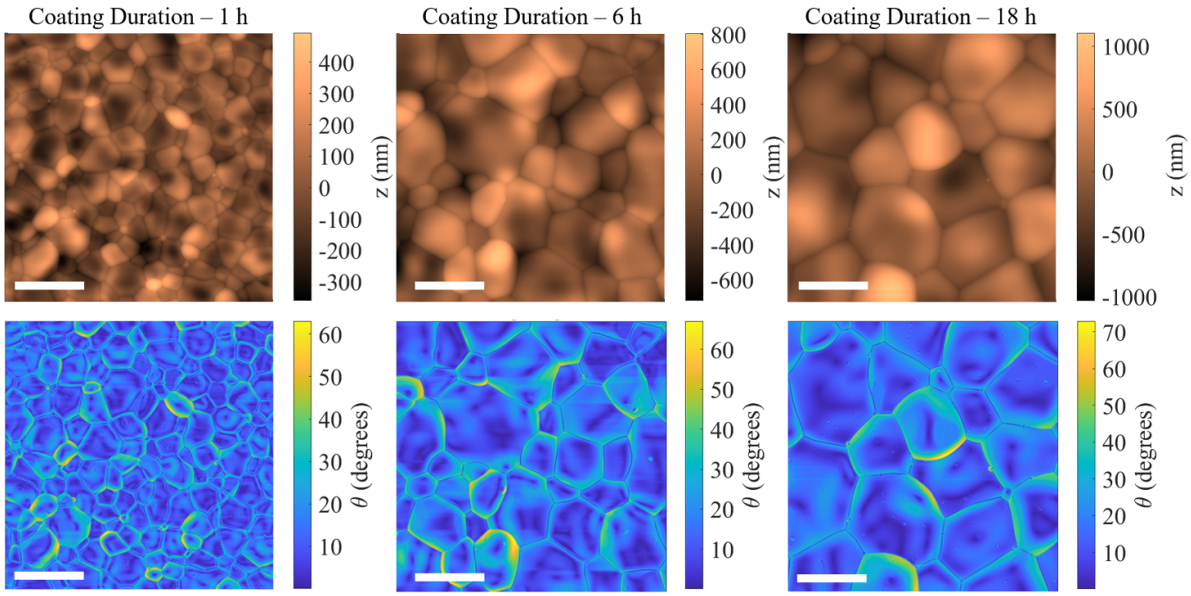

Figure 3. Representative TMAFM topographies (upper panels) and slope angles (lower panels) showing the evolution of Nb_3Sn topography with coating duration. The scale bars are 5 μm.

which is computed numerically. This model predicts a SFS factor based on the slope angle of the groove, θ, the depth of the groove, δ, the superconductor's coherence length, ξ, and the London penetration depth, λ. This model spans from the nanoscale limit considered by Kubo [22] to the deep groove geometry considered by Buzdin and Daumens [37] and can be used between the two limits where many of the defects in the Nb_3Sn system find themselves. Using equation (6) and estimating $\xi \approx 3$ nm and $\lambda \approx 120$ nm for Nb_3Sn [38–40], $\eta(\delta,\theta)$ is plotted in figure 2(b). The superconducting coherence length and penetration depth values used are qualitatively useful for evaluating the effect of surface roughness on the superheating field for other materials [41]. The surface in figure 2(b) shows that the SFS factor can be quickly degraded by defects of only a few 10's of nanometers deep and slope angles exceeding 10°. In the limit of deep grooving, the SFS factor ceases to change with increasing depth of the groove, which is consistent with the deep groove limit [37]. The slope angle dependent deep-groove limit SFS factors for this model are plotted in figure 2(c).

The topographic evolution of Nb_3Sn with coating durations between 1–78 h was examined. Ten topographic measurements sampled randomly across the surface of each sample were made at 20 μm × 20 μm for samples coated up to 18 h and at 25 μm × 25 μm for 60 h and 78 h. Representative TMAFM images are shown in figure 3. Extended coatings develop on average larger grains and increased peak-to-valley distance as indicated by the z color scale in figure 3. Local slope angles can be very large, exceeding 60° in some cases. As shown in figure 3, the largest slope angles form exclusively between particularly tall grains and much shorter ones. As measured by TMAFM, large slope angles tend to form a slope-angled step geometry but could have more complex geometry not apparent to AFM [42]. MFE factor maps are calculated using the methods outlined in previous work [29]. The SFS factor maps are calculated similar to that in [29] by determining $\delta(\mathbf{r})$ and $\theta(\mathbf{r})$ as inputs to equation (6). We estimate $\delta(\mathbf{r})$ by taking the difference between the topography and a plane formed by a first order, 11-pixel frame, Savitzky–Golay type [43, 44] smoothing of the topography. This serviceable estimate of $\delta(\mathbf{r})$ tends to underestimate δ due to the nature of the smoothing procedure on the complex topography of Nb_3Sn. MFE and SFS factor maps derived from the topography in figure 4(a) are shown in figures 4(b) and (c). As shown in figure 4(c), the grain boundary grooves host the most severely degraded superheating field suppression factors. Considering the combined effect of SFS and MFE on maximum supportable field, $B^*_{\mathrm{max}}(\mathbf{r}) = (\eta/\beta)B_{\mathrm{max}}$, the SFS factors are at least $\sim 2\times$ more severe than the MFE factors observed in figure 4(b) which may account for a substantial reduction in peak supportable magnetic field in Nb_3Sn films since only a small fraction of vortex-active grain boundaries are required to increase surface resistance substantially [28].

The relative frequencies of parameters extracted from the AFM topographies are shown in figure 5. The distribution of $\theta(\mathbf{r})$ and $\delta(\mathbf{r})$ is shown in figures 5(a) and (b). No discernible trend with coating duration is observed in the distribution of $\theta(\mathbf{r})$, while the depth of the grooves, represented by the high-δ branch, tends to increase with increasing coating duration, as shown in figure 5(b). These observations are qualitatively consistent with the thermal grooving of grain boundaries where the dihedral angle is often assumed not to change [34] or expected to change very little [45] during high temperature annealing. The distribution of peak local MFE factors, shown in figure 5(c), also does not show any discernible trend as coating duration increases, which is likely due to the self-similar

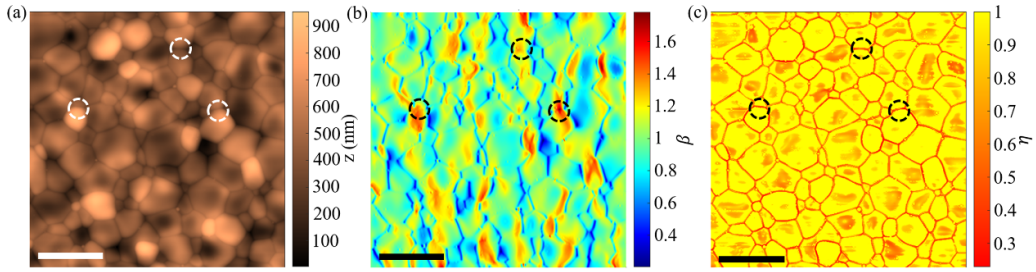

Figure 4. (a) Representative topography of a Nb_3Sn sample coated at 1200 °C for 3 h. (b) MFE factor map of the topography used in (a). (c) SFS factor map of the topography used in (a). Dashed circles indicate some of the regions on the surface where SFS and MFE coincide. The scale bars are 5 μm.

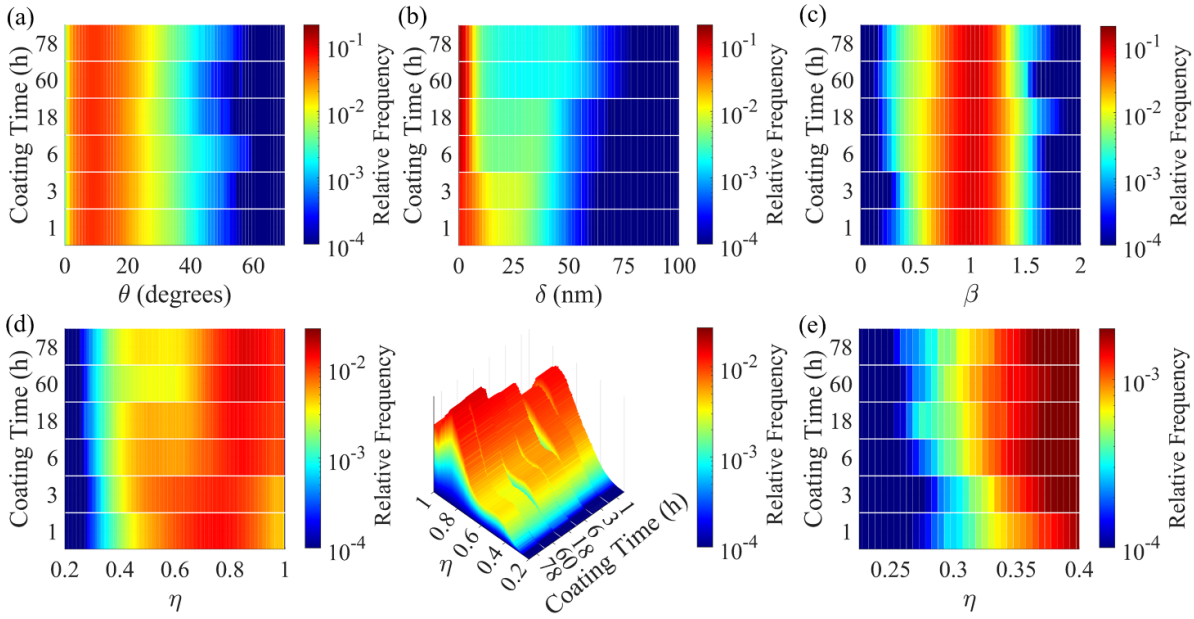

Figure 5. (a) Relative frequencies of local slope angle, θ, (b) deviation between topography and background plane, δ, (c) local MFE factors, β, (d) local SFS factors, η, and a tilted view showcasing the low-η bifurcation, and (e) a zoom-in of the low-η SFS factors highlighting the effect of deepening thermal grooves with coating duration. The relative frequency cutoff of 10^{-4} corresponds to the significance of a 630 × 630 nm^2 patch for the 20 μm × 20 μm data sets.

growth of thermal grooves. Peak MFE factors fall between 1.5 and 2 in agreement with previous estimates of MFE factors on Nb_3Sn [46]. It is worth reiterating that the MFE factors obtained here were calculated in the framework of the perfect electrical conductor model, which assumes the limit $\lambda \to 0$, however the length scale of the defects is in fact comparable to the London penetration depth of Nb_3Sn of ∼120 nm. The comparative length scale effectively reduces the severity of MFE near sharp edges which would otherwise diverge in the perfect electrical conductor model. The SFS factors distributions shown in figure 5(d) presents a merged bimodal distribution that bifurcates as coating duration increases. This bifurcation is also reflected in the δ distribution in figure 5(b). The low-η branch, related to the grain boundary grooving process, widens and extends toward lower-η values and lower relative frequency. The extension to lower-η values is due to the increasing depth of grain boundary grooves, while its decrease in relative frequency is due to the reduced sampling of grain boundaries in the scan areas caused by grain growth during extended coating duration. A zoom-in on low-η values is presented in figure 5(e), which shows that the low-η distribution reaches from $\eta \sim 0.3$ for short coating times to $\eta \sim 0.25$ for longer coating times. Despite the deepening of grooves in figure 5(b), the SFS factors stabilize and do not further decrease. This is due to the invariance of SFS factors on groove depth in the deep-groove limit as shown in figure 2(b). Considering a theoretical superheating field of ≈400 mT for Nb_3Sn and the value of SFS factors alone, this would correspond to accelerating fields from ∼25–30 MV m^{-1} (107–128 mT) in TESLA-shaped cavities [47]. Additional loss in peak field may be observed if MFE and SFS coincide. Such locations, some of which are circled in figures 4(a)–(c), may further reduce the peak accelerating field by a factor of ∼1.7, yielding ∼12–18 MV m^{-1} (51–77 mT). While this is in qualitative agreement with the field limitation observed in Nb_3Sn cavities, we expect that the London model estimation of the SFS factors represents a lower bound of η due to nonlocality of the BCS current-field relation. Additional causes of

performance degradation are likely concurrent. Performance limiting mechanisms may take the form of Sn droplets [48], thin patchy regions [49], reduced thermal conductivity [50] or weak links caused by non-stoichiometry at grain boundaries [28, 51, 52]. Recent calculations suggest that thermal conductivity is not currently a limiting factor in typically grown, few-μm thick films [53]. Based on this, these topographic defects may account for a substantial degradation of peak-field in dense and stoichiometric Nb_3Sn thin films grown via Sn vapor diffusion. If possible, groove slope angles and groove depths should be minimized to preserve the superheating field as shown in figure 2(b). Coating duration should be optimized to minimize further degradation of SFS and MFE factors via thermal grooving. However, the coating must satisfy other conditions, like a minimum film thickness and uniformity which may not necessarily coincide with shortened coating duration.

In summary, we have investigated the effects of coating growth duration on the topography of vapor-diffused Nb_3Sn grown at 1200 °C. Within the perfect electrical conductor model and SFS model based on the London theory, we have shown that thermal grooves are particularly severe for SFS, and the effects of MFE are non-negligible but comparatively smaller. We expect improved estimations of SFS to be obtained from the Ginzburg-Landau theory using realistic superconducting properties, but this method quickly becomes computationally expensive for high λ/ξ material [23]. These thermal grooves should act as gates for vortices to enter the superconductor and limit achievable fields. It is imperative to seek processes that reduce groove slope angles and groove depths to mitigate performance degradation due to geometrical SFS. It may be possible to modify or inhibit the thermal grooving process via surface energy anisotropy [54] or introducing impurities [55], however, care must be taken not to reduce the coherence length substantially, making the film even more susceptible to SFS [22, 37]. In contrast to our present investigation, previous work showed that Nb_3Sn grown at different temperatures presented different distributions of MFE [56]. This suggests that growth temperature may have a sizable effect on the surface morphology. Exploring the effect of growth temperature as well as comparing RF performance with topography of witness samples is a natural next step. Additional post processing may be possible. Electropolishing [57], oxypolishing [58, 59], and centrifugal barrel polishing [60] may offer avenues to reduce the effects of surface roughness.

Data availability statement

All data that support the findings of this study are included within the article (and any supplementary files).

Acknowledgments

This material is based upon work supported by the U.S. Department of Energy, Office of Science, Office of Nuclear Physics under Contract DE-AC05-06OR23177. This work was supported in part by the U.S. Department of Energy, Office of Science, Office of Workforce Development for Teachers and Scientists (WDTS) under the Science Undergraduate Laboratory Internships (SULI) program as well as the U.S. National Science Foundation Research Experience for Undergraduates at Old Dominion University Grant No. 2348822. We gratefully acknowledge G Eremeev and M Kelley for their support to fabricate samples used in this work. We are grateful to C Reece for insightful discussions.

ORCID iDs

Eric M Lechner https://orcid.org/0000-0002-0517-5702
Jonathan W Angle https://orcid.org/0000-0002-7097-0024
Uttar Pudasaini https://orcid.org/0000-0002-0535-8453

References

[1] DeSorbo W 1963 Effect of dissolved gases on some superconducting properties of niobium *Phys. Rev.* **132** 107–21
[2] Ciovati C 2013 Where next with SRF? *Proc. IPAC 2013* pp 3124–8
[3] Matricon J and Saint-James D 1967 Superheating fields in superconductors *Phys. Lett.* A **24** 241–2
[4] Lechner E M, Oli B D, Makita J, Ciovati G, Gurevich A and Iavarone M 2020 Electron tunneling and x-ray photoelectron spectroscopy studies of the superconducting properties of nitrogen-doped niobium resonator cavities *Phys. Rev. Appl.* **13** 044044
[5] Godeke A 2006 A review of the properties of Nb_3Sn and their variation with A15 composition, morphology and strain state *Supercond. Sci. Technol.* **19** R68
[6] Posen S and Liepe M 2014 Advances in development of Nb_3Sn superconducting radio-frequency cavities *Phys. Rev. ST Accel. Beams* **17** 112001
[7] Keckert S *et al* 2019 Critical fields of Nb_3Sn prepared for superconducting cavities *Supercond. Sci. Technol.* **32** 075004
[8] Moore D F, Zubeck R B, Rowell J M and Beasley M R 1979 Energy gaps of the $A-15$ superconductors Nb_3Sn, V_3Si and Nb_3Ge measured by tunneling *Phys. Rev.* B **20** 2721–38
[9] Kephart R D *et al* 2015 SRF, compact accelerators for industry & society *Proc. Int. Conf. on RF Superconductivity (SRF2015), (Whistler, BC, Canada, 13 September-18 September 2015)* (*Int. Conf. on RF Superconductivity*) pp 1467–73
[10] Barletta William A and Borland M 2010 Report of the basic energy sciences workshop on compact light sources *Technical Report*
[11] Posen S, Valles N and Liepe M 2015 Radio frequency magnetic field limits of Nb and Nb_3Sn *Phys. Rev. Lett.* **115** 047001
[12] Posen S and Hall D L 2017 Nb_3Sn superconducting radiofrequency cavities: fabrication, results, properties and prospects *Supercond. Sci. Technol.* **30** 033004
[13] Posen S, Lee J, Seidman D N, Romanenko A, Tennis B, Melnychuk O S and Sergatskov D A 2021 Advances in Nb_3Sn superconducting radiofrequency cavities towards first practical accelerator applications *Supercond. Sci. Technol.* **34** 025007

[14] Knobloch J, Geng R L, Liepe M and Padamsee H 1999 High-field Q slope in superconducting cavities due to magnetic field enhancement at grain boundaries *Proc. 9th Workshop on RF Superconductivity* pp 77–91

[15] Xu C, Reece C E and Kelley M J 2016 Simulation of nonlinear superconducting rf losses derived from characteristic topography of etched and electropolished niobium surfaces *Phys. Rev. Accel. Beams* **19** 033501

[16] Gurevich A 2006 Multiscale mechanisms of SRF breakdown *Physica* C **441** 38–43

[17] Kubo T 2015 Magnetic field enhancement at a pit on the surface of a superconducting accelerating cavity *Prog. Theor. Exp. Phys.* **2015** 073G01

[18] Shemelin V and Padamsee H 2008 Magnetic field enhancement at pits and bumps on the surface of superconducting cavities *TTC-Report* 2008

[19] Xie Y, Liepe M and Padamsee H 2011 Quench simulation using a ring-type defect model *Proc. SRF'11* pp 687–90

[20] Xie Y and Liepe M 2013 Quench and field dependent surface resistance studies using a single cell cavity with artificial pits *Proc. SRF'13* pp 378–91

[21] Aladyshkin A Y, Mel'Nikov A S, Shereshevsky I A and Tokman I D 2001 What is the best gate for vortex entry into type-II superconductor? *Physica* C **361** 67–72

[22] Kubo T 2015 Field limit and nano-scale surface topography of superconducting radio-frequency cavity made of extreme type II superconductor *Prog. Theor. Exp. Phys.* **2015** 63G01-0

[23] Pack A R, Carlson J, Wadsworth S and Transtrum M K 2020 Vortex nucleation in superconductors within time-dependent Ginzburg-Landau theory in two and three dimensions: role of surface defects and material inhomogeneities *Phys. Rev.* B **101** 144504

[24] Clem J R and Berggren K K 2011 Geometry-dependent critical currents in superconducting nanocircuits *Phys. Rev.* B **84** 174510

[25] Hortensius H L, Driessen E F C, Klapwijk T M, Berggren K K and Clem J R 2012 Critical-current reduction in thin superconducting wires due to current crowding *Appl. Phys. Lett.* **100** 182602

[26] Gurevich A and Ciovati G 2008 Dynamics of vortex penetration, jumpwise instabilities and nonlinear surface resistance of type-II superconductors in strong RF fields *Phys. Rev.* B **77** 104501

[27] Gurevich A 2012 Superconducting radio-frequency fundamentals for particle accelerators *Rev. Accel. Sci. Technol.* **5** 119–46

[28] Carlson J *et al* 2021 Analysis of magnetic vortex dissipation in Sn-segregated boundaries in Nb_3Sn superconducting RF cavities *Phys. Rev.* B **103** 024516

[29] Lechner E M, Angle J W, Baxley C, Kelley M J and Reece C E 2023 Topographic evolution of heat-treated Nb upon electropolishing for superconducting rf applications *Phys. Rev. Accel. Beams* **26** 103101

[30] Lechner E M, Angle J W, Palczewski A D, Stevie F A, Kelley M J and Reece C E 2024 Oxide dissolution and oxygen diffusion scenarios in niobium and implications on the Bean–Livingston barrier in superconducting cavities *J. Appl. Phys.* **135** 133902

[31] Pudasaini U, Eremeev G V, Angle J W, Tuggle J, Reece C E and Kelley M J 2019 Growth of Nb_3Sn coating in tin vapor-diffusion process *J. Vac. Sci. Technol.* A **37** 051509

[32] Pudasaini U, Eremeev G V, Reece C E, Tuggle J and Kelley M J 2019 Initial growth of tin on niobium for vapor diffusion coating of Nb_3Sn *Supercond. Sci. Technol.* **32** 045008

[33] This silicon nitride probe features a single V-shaped, Al reflex coated cantilever with low spring constant (nominal 0.4 N/m). Nominal tip radius of 2 nm, with front, back and side nominal angles of 15°, 25° and 17.5° degrees, respectively.

[34] Mullins W W 1957 Theory of thermal grooving *J. Appl. Phys.* **28** 333–9

[35] Akyildiz O and Ogurtani T O 2017 Thermal grooving by surface diffusion: a review of classical thermo-kinetics approach *Hittite J. Sci. Eng.* **4** 7–16

[36] Bean C P and Livingston J D 1964 Surface barrier in type-II superconductors *Phys. Rev. Lett.* **12** 14–16

[37] Buzdin A and Daumens M 1998 Electromagnetic pinning of vortices on different types of defects *Physica* C **294** 257–69

[38] Posen S 2015 Understanding and overcoming limitation mechanisms in Nb_3Sn superconducting RF cavities *PhD Thesis* Cornell University

[39] Liarte D B, Posen S, Transtrum M K, Catelani G, Liepe M and Sethna J P 2017 Theoretical estimates of maximum fields in superconducting resonant radio frequency cavities: stability theory, disorder and laminates *Supercond. Sci. Technol.* **30** 033002

[40] Hall D L 2017 New insights into the limitations on the efficiency and achievable gradients in Nb_3Sn SRF cavities *PhD Thesis* Cornell University

[41] Valente-Feliciano A -M 2016 Superconducting RF materials other than bulk niobium: a review *Supercond. Sci. Technol.* **29** 113002

[42] Lee J, Posen S, Mao Z, Trenikhina Y, He K, Hall D L, Liepe M and Seidman D N 2018 Atomic-scale analyses of Nb_3Sn on Nb prepared by vapor diffusion for superconducting radiofrequency cavity applications: a correlative study *Supercond. Sci. Technol.* **32** 024001

[43] Kuo J E, Wang H and Pickup S 1991 Multidimensional least-squares smoothing using orthogonal polynomials *Anal. Chem.* **63** 630–5

[44] Savitzky A and Golay M J E 1964 Smoothing and differentiation of data by simplified least squares procedures *Anal. Chem.* **36** 1627–39

[45] Zhang W, Sachenko P and Schneibel J H 2002 Kinetics of thermal grain boundary grooving for changing dihedral angles *J. Mater. Res.* **17** 1495–501

[46] Porter R D, Hall D L, Liepe M and Maniscalco J T 2017 Surface roughness effect on the performance of Nb_3Sn cavities *JACoW* (*Linear Accelerator Conf.*) pp 129–32

[47] Aune B *et al* 2000 Superconducting TESLA cavities *Phys. Rev. ST Accel. Beams* **3** 092001

[48] Jiang G *et al* 2024 Understanding and optimization of the coating process of the radio-frequency Nb_3Sn thin film superconducting cavities using tin vapor diffusion method *Appl. Surf. Sci.* **643** 158708

[49] Pudasaini U, Eremeev G, Kelley M, Reece C and Tuggle J 2017 Surface studies of Nb_3Sn coated samples prepared under different coating conditions *18th Int. Conf. on RF Superconductivity* pp 894–9

[50] Cody G D and Cohen R W 1964 Thermal conductivity of Nb_3Sn *Rev. Mod. Phys.* **36** 121–3

[51] Sandim M J R, Tytko D, Kostka A, Choi P, Awaji S, Watanabe K and Raabe D 2013 Grain boundary segregation in a bronze-route Nb_3Sn superconducting wire studied by atom probe tomography *Supercond. Sci. Technol.* **26** 055008

[52] Lee J, Mao Z, He K, Sung Z H, Spina T, Baik S -I, Hall D L, Liepe M, Seidman D N and Posen S 2020 Grain-boundary structure and segregation in Nb_3Sn coatings on Nb for high-performance superconducting radiofrequency cavity applications *Acta Mater.* **188** 155–65

[53] Kulyavtsev P, Eremeev G and Posen S 2021 Simulations of Nb_3Sn layer RF field limits due to thermal impedance 2104.01267

[54] Rabkin E, Gabelev A, Klinger L, Semenov V N and Bozhko S I 2006 Grain boundary grooving in molybdenum bicrystals *J. Mater. Sci.* **41** 5151–60
[55] Iwasaki T, Sasaki N, Yasukawa A and Chiba N 1997 Molecular dynamics study of impurity effects on grain boundary grooving *JSME Int. J.* A **40** 15–22
[56] Pudasaini U, Kelley M J, Lechner E M, Reece C E, Trofimova O and Valente-Feliciano A-M 2023 Surface roughness reduction and performance of vapor-diffusion coating of Nb_3SN film for SRF application *Int. Conf. on RF Superconductivity (Geneva, Switzerland)* (JACoW) pp 593–9
[57] Pudasaini U, Eremeev G V, Kelley M J, Reece C E and Tian H 2018 Electrochemical finishing treatment of Nb_3Sn diffusion-coated niobium *Proc. Int. Conf. on RF Superconductivity (SRF'17), (Lanzhou, China, 17 July-21 July 2017)* (*Int. Conf. on RF Superconductivity*) (JACoW) pp 900–5
[58] Pudasaini U, Eremeev G V, Kelley M J, Reece C E and Tuggle J 2017 Post-Processing of Nb_3Nn Coated Nb *Proc. Int. Particle Accelerator Conf. (IPAC'17) (Copenhagen, Denmark, May 2017)* (*Int. Particle Accelerator Conf.*) (JACoW) pp 1190–3
[59] Porter R D, Furuta F, Hall D L, Liepe M and Maniscalco J T 2017 Effectiveness of chemical treatments for reducing the surface roughness of Nb_3Sn *Int. Particle Accelerator Conf.* (JACoW) pp 1145–8
[60] Viklund E, Seidman D N, Burk D and Posen S 2024 Improving Nb_3Sn cavity performance using centrifugal barrel polishing *Supercond. Sci. Technol.* **37** 025009